Estuarine, Coastal and Shelf Science 341 (2026) 110140

Contents lists available at ScienceDirect

Estuarine, Coastal and Shelf Science

journal homepage: www.elsevier.com/locate/ecss

Diagnosis of residual flow drivers in estuaries with the densimetric tidal Froude number

M. Khosravi [a,e,*], A.B. Fortunato [b], A. Lopez-Ruiz [c], A. Valle-Levinson [d], E. Garel [a]

[a] CIMA/ARNET, Universidade do Algarve, Faro, Portugal
[b] LNEC – Laboratório Nacional de Engenharia Civil, Avenida do Brasil 101, Lisboa, 1700-066, Portugal
[c] Departamento de Ingeniería Aeroespacial y Mecánica de Fluidos, Universidad de Sevilla, Camino de los Descubrimientos s/n, Seville, 41092, Spain
[d] Civil and Coastal Engineering Department, University of Florida, Gainesville, USA
[e] Department of Civil and Resource Engineering, Dalhousie University, 5268 DaCosta Row, Halifax, Nova Scotia, B3H 4R2, Canada

ARTICLE INFO

Keywords:
Estuarine hydrodynamics
3D numerical model
Densimetric tidal Froude number

ABSTRACT

Residual circulation in estuaries drives salt intrusion, material transport, and ecosystem functioning. Yet the ability to diagnose its dominant forcing mechanism remains a challenge. While previous studies suggest that the densimetric tidal Froude number (Fr_t) may distinguish tidal from baroclinic forcing, its reliability across varying estuarine conditions and spatial scales requires systematic evaluation. This study carries out such evaluation with a suite of process-oriented numerical simulations in an idealized estuary–shelf system that features Gaussian cross-channel bathymetry. Here, Fr_t is treated as a diagnostic indicator reflecting the dynamics established by either barotropic or baroclinic forcing. The model configuration spans a parameter space that includes variations in tidal amplitude, channel depth, lateral slope, and river discharge. Residual circulation regimes are diagnosed using the ratio between the barotropic and baroclinic terms of the tidally averaged, axial momentum equation obtained from model outputs. Diagnoses are made together with the transverse structure of residual flows, allowing direct comparison with Fr_t predictions. This study demonstrates that Fr_t can reliably diagnose the dominant driver of residual circulation when the density length scale is defined over the shortest feasible axial distances. Crucially, the results show that the skill of Fr_t is highly sensitive to this spatial scale: its performance deteriorates when the density gradient is computed over lengths that extend into regions with heterogeneous forcing. Across all simulations, Fr_t functions as a robust bulk indicator of tide-dominated, density-dominated, or regimes influenced by both forcings only when the density scale is restricted to zones where the axial density gradient is approximately constant. Such zones consistently occupy the seaward side of the peak salinity gradient. Within this region, Fr_t emerges as a relevant diagnostic tool and offers process-oriented guidance for results that require identifying the prevailing residual-flow driver. The experiments suggest configuration-dependent Fr_t ranges associated with regimes dominated by tides, density gradients, or both.

1. Introduction

Estuarine subtidal circulation is governed by the interaction among density gradient (linked to freshwater inflow), tides, and wind forcing. These processes together determine stratification and turbulent mixing, and are molded by estuarine geometry (Hansen and Rattray, 1966; Pingree and Maddock, 1977; Jay and Smith, 1990a, 1990b; Friedrichs and Hamrick, 1996; Geyer and MacCready, 2014, Valle-Levinson, 2021). In many estuaries, the interaction leads to the dominance of either density-driven or tidally induced circulation, or they interact to control the net subtidal transport (Li et al., 1998; Valle-Levinson et al., 2000; Valle-Levinson and Schettini, 2016). This subtidal (or tidally averaged) circulation plays a central role in controlling the distribution and transport of salt, nutrients, sediments, and pollutants within estuaries, thereby linking physical processes to ecosystem functioning (Gardner and Kjerfve, 2006). In idealized rectangular cross-sections, gravitational circulation, characterized by seaward surface flow and landward bottom flow (Pritchard, 1956; Hansen and Rattray, 1966), competes with the tidally induced residual flow, which tends to be landward at the surface and seaward below due to tidal nonlinearities (Ianniello, 1977a; b). In estuaries with lateral depth variation, baroclinic exchange flows are laterally sheared, with landward flow in deeper

* Corresponding author. CIMA/ARNET, Universidade do Algarve, Faro, Portugal.
E-mail address: mkhosravi@ualg.pt (M. Khosravi).

https://doi.org/10.1016/j.ecss.2026.110140
Received 20 March 2026; Received in revised form 16 July 2026; Accepted 20 July 2026
Available online 22 July 2026

channels and seaward flow over shoals (Wong, 1994; Valle-Levinson, 2008). Tidally induced flows in long estuarine channels are in the opposite direction, with landward flow over shoals and seaward flow in channels (Li and O'Donnell, 2005). The competition between tidal and baroclinic forcings can therefore occur in both the vertical and lateral planes, with the resulting structure determined by the dominant forcing.

Identifying the dominant forcing in estuaries provides insight into how an estuary responds to tidal modulation, freshwater inflow, and climate variability (Cho et al., 2020; Valle-Levinson and Schettini, 2016). Observations from subtropical, semi-arid, and temperate estuaries indicate that the primary drivers of residual flow—such as horizontal density gradients and tidal stresses—can alternate on fortnightly or seasonal timescales (Garel and Ferreira, 2013; Valle-Levinson and Schettini, 2016; Ross et al., 2017). Systematic numerical experiments further confirm the flow alternation over such timescales (Khosravi et al., 2025). Valle-Levinson and Schettini (2016) further proposed that the main driver of the residual circulation can be effectively diagnosed using the densimetric tidal Froude number (Fr_t), a non-dimensional parameter derived from scaling of the tidally averaged momentum balance, which distinguishes tidally dominated ($|Fr_t| \gg 1$) from density-driven ($|Fr_t| \ll 1$) conditions. However, despite its conceptual appeal, no studies have evaluated the efficacy of Fr_t in predicting the dominant driving mechanism of residual circulation, particularly regarding the appropriate spatial length scales to use when applying this parameter.

This study aims to systematically evaluate the reliability of Fr_t as a diagnostic indicator of the dominant mechanisms, density gradients or tides, driving residual circulation along an estuary. Using process-oriented numerical simulations in an idealized shelf–estuary system with Gaussian-shaped cross-channel bathymetry, tidal and buoyancy forcing are varied across a wide range of conditions and spatial locations. This controlled setup enables a comprehensive examination of how the dominant forcing and corresponding residual circulation patterns agree with the prediction of Fr_t. Here, Fr_t is treated as a diagnostic indicator reflecting the dynamics established by either barotropic or baroclinic forcing. The results provide process-oriented guidance for field observations, particularly for studies where the knowledge of the dominant driver is relevant.

The remainder of the paper is organized as follows. Section 2 introduces the theoretical background of Fr_t and distinguishes it from other Froude numbers. Section 3 describes the methodology, including the numerical model configuration and the nondimensional parameters adopted in this study. Section 4 presents the results, examining a range of estuarine conditions and scenarios and assessing whether Fr_t number can diagnose the dominant forcing across all experiments. These results are interpreted and discussed in Section 5 through comparison with previous applications of Fr_t in field observations. Finally, Section 6 summarizes the main conclusions.

2. The densimetric tidal Froude number

In the context of estuarine dynamics, the classical Froude number is defined as

$$Fr = \frac{u}{\sqrt{gH}} \tag{1}$$

the ratio between the instantaneous flow speed (u) and the celerity of the tidal wave which depends on the mean water depth H and gravitational acceleration g (Dyer, 1973). The Froude number distinguishes the dynamical flow regimes (supercritical or subcritical), indicating whether tidal waves can propagate upstream, against the river flow. The densimetric Froude number (e.g., Farmer and Smith, 1980), defined as

$$F_i = \frac{u_T}{c_i} \tag{2}$$

relates the instantaneous, sectionally averaged, barotropic tidal speed u_T (m/s) to the long internal wave celerity c_i (m/s), for mode i, over topographic constrictions such as sills. It is useful to identify conditions under which internal wave dynamics can lead to enhanced mixing. Furthermore, Geyer (2010) developed a scaling framework relating riverine and tidal forcing to estuarine stratification, which was later expressed in nondimensional form using Froude numbers. The densimetric estuarine Froude number is

$$F_R = \frac{u_R}{\sqrt{g\beta S_0 H}} \tag{3}$$

and the tidal Froude number is

$$F_T = \frac{u_T}{\sqrt{g\beta S_0 H}} \tag{4}$$

where u_R the river velocity (m/s), β is the haline contraction coefficient, S_0 is representative ocean salinity (g/kg). These parameters express the relative importance of riverine (F_R) and tidal (F_T) forcing to the baroclinic internal wave speed $\sqrt{g\beta S_0 H}$, which provides a characteristic velocity scale for the stratification response. To account for estuarine geometry, Guha and Lawrence (2013) further introduced the modified tidal Froude number

$$\widetilde{F}_T = F_T\sqrt{\frac{B}{H}} = \frac{u_T}{\sqrt{g\beta S_0 H}}\sqrt{\frac{B}{H}} \tag{5}$$

where B is the estuarine width (m). This formulation incorporates the aspect ratio B/H, recognizing that wider estuaries facilitate enhanced lateral mixing and thus greater tidal influence. Collectively, F_R and $\widetilde{F}_T$ quantify the competition between riverine buoyancy input and tidal stirring that governs the degree of estuarine stratification, from well-mixed to salt-wedge regimes. Although these parameters characterize the competition between riverine buoyancy input and tidal stirring that controls stratification, they do not directly quantify the balance of forces driving residual circulation.

Along-estuary residual flow dynamics can be approximated with the effects of pressure gradients, tidal stresses, and frictional forces, neglecting local accelerations, vertical velocities, horizontal friction, Coriolis forces, and wind forcing (Valle-Levinson and Schettini, 2016). Within this framework, the mass balance ensures that water level slopes adjust to density gradients and tidal forcing (e.g., Officer, 1976; Li and Valle-Levinson, 1999; Li and O'Donnell, 2005). As a result, the relative contribution of residual flow drivers can be quantified by comparing the scaled baroclinic pressure gradient with the scaled tidal stress (Valle-Levinson and Schettini, 2016; Valle-Levinson, 2021, 2022). The derived parameter, the densimetric tidal Froude number (Fr_t), quantifies the relative importance of baroclinic versus barotropic processes, and is expressed as

$$Fr_t = (L_\rho / L_T)\left(U_0{}^2 / g'\mathrm{H}\right) \tag{6}$$

where U_0 is the tidal velocity amplitude at the thalweg, and $g' = g\,\Delta\rho_h/\rho_0$ is the reduced gravity, and ρ_0 a reference density. The horizontal tidal length scale, L_T, is commonly defined as the tidal excursion over half a tidal cycle, given by $(U_0 T)/\pi$, where T denotes the tidal period. The density difference $\Delta\rho_h$, which retains the sign of the reduced gravity, is defined over the horizontal density length scale L_ρ (Valle-Levinson, 2022).

Since Fr_t is based on the reduced gravity, it compares tidal flow amplitude to the celerity of stratification-controlled (internal) gravity waves ($\sqrt{g'\mathrm{H}}$), which is the defining characteristic of a densimetric Froude number (Dyer, 1973). The definition of Fr_t implicitly assumes constant eddy viscosity and therefore does not represent eddy viscosity–shear covariance circulation (ESCO; (Dijkstra et al., 2017)). Instead, it indicates the dominant balance between tidal and baroclinic forcing.

The practical application of Fr_t hinges on the choice of the density length scale L_ρ, which is uncertain and has garnered less attention than the formulation of Fr_t itself. In estuaries, where horizontal salinity gradients are often non-linear, the choice of L_ρ becomes important, whereas it is less critical for a linear density gradient. For example, if L_ρ is defined over the salinity intrusion length, it may encompass regions with very different density gradients, leading to a bulk Fr_t which is not representative of local values. Identifying optimal length scales would support the design of observational studies of residual flow dynamics, providing guidance about locations for in-situ measurements of the axial salinity gradient. So far, such studies have adopted different approaches for defining this characteristic scale, dictated by the spatial resolution and extent of available field observations. Valle-Levinson and Schettini (2016) assumed comparable tidal and baroclinic length scales in the Mossoró Estuary (Brazil). Cho et al. (2020) defined the density-gradient length scale based on the spatial extent of observations in the Sumjin River Estuary (South Korea). In the Gironde Estuary (France), Ross et al. (2017) also assumed comparable tidal and baroclinic length scales to investigate the drivers of transverse subtidal variability over the spring–neap cycle. More recently, Garel et al. (2025), using fortnightly observations from the Guadiana Estuary (Portugal), showed that Fr_t was consistent with the observed fortnightly reversal in the lateral structure of residual flows when L_ρ accounts for local spatial variations in the density gradient. Thus, a key question being addressed in the present study is: over what along-channel distance should the density gradient be measured to reliably compute Fr_t and diagnose the dominant residual flow mechanisms?

3. Methods

3.1. Numerical model

Model simulations were conducted using the Delft3D FLOW (Lesser et al., 2004), a high-resolution, process-based model well-suited for a broad range of riverine, estuarine, and coastal environments. The model solves the Reynolds-averaged shallow-water equations, derived from the Navier–Stokes equations for incompressible, free-surface flows. It also includes a transport equation for salinity and applies a k–ε turbulence closure scheme. Further details on the hydrodynamic equations and their implementation can be found in Deltares (2013).

The numerical model is implemented within a computational domain that idealizes a coupled shelf–estuarine channel system (Fig. 1a and b). The horizontal grid consists of 260 nodes in the along-channel direction and 100 nodes in the cross-shelf direction, with 20 vertical sigma layers. The continental shelf spans 24 km in width, featuring a cross-shelf bottom slope of 0.0025, and extends 15 km offshore, corresponding to a grid of 26 by 100 cells. Numerical simulations demonstrated that the shelf is wide enough to prevent boundary condition effects from influencing the results in the estuary, and that the model effectively exports estuarine water through the open shelf boundaries during ebb tides. The estuarine channel measures 1 km in width, has straight lateral boundaries, and stretches 80 km inland with a gentle bottom slope of 10^{-5} in the along-channel direction (Fig. 1c). This configuration translates to 240 grid cells along ($\Delta x \approx 333$ m) and 15 cells across the estuary ($\Delta y \approx 67$ m). The channel length was

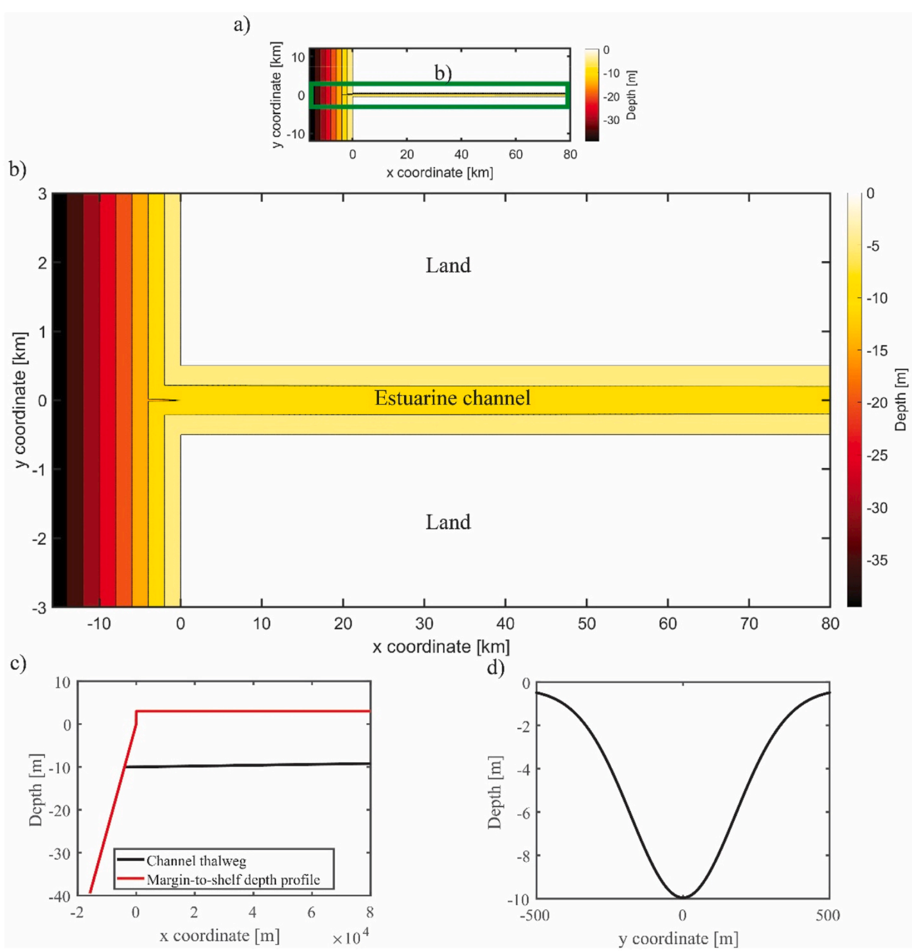

Fig. 1. Bathymetric map and domain configuration for the control experiment (see Table 1). (a) Shelf-estuary bathymetry. (b) Enlarged view of the green box highlighted in (a). (c) Schematic representation of the model domain and bathymetry and (d) Cross-channel geometry. (For interpretation of the references to color in this figure legend, the reader is referred to the Web version of this article.)

sufficient to eliminate numerical artifacts from the upstream boundary and to fully resolve the interaction between river discharge and tidal dynamics. As most studies about residual flow dynamics (e.g., Burchard et al., 2011; Li and O'Donnell, 2005; Valle-Levinson, 2008), the cross-channel bathymetry is idealized as a Gaussian profile to represent a central channel flanked by shoals (Fig. 1c), expressed as:

$$H(y) = H_{max}\, exp\left(-\frac{(y-y_0)^2}{2c^2}\right) \tag{7}$$

Here, H_{max} denotes the maximum depth at the estuary mouth, y_0 represents the centerline position of the Gaussian profile, and c is the standard deviation characterizing the lateral depth distribution. In this study, a minimum depth of 0.5 m relative to mean sea level was imposed at the channel margins, with y_0 positioning the thalweg at the midpoint of the cross-section. The Gaussian bathymetry was adopted because it captures the characteristic channel-shoals morphology of coastal-plain estuaries. This idealized configuration is widely used to investigate estuarine residual circulation while minimizing site-specific geometric complexities (Li and O'Donnell, 2005; Hosseini et al., 2023; Khosravi et al., 2025).

A value of 0.0003 m^2/s was selected for both the background vertical eddy diffusivity and viscosity, informed by sensitivity analyses. Deviations from this value resulted in unrealistic along-channel salinity distributions and introduced noise in the residual flow time series. In addition, bottom friction was parameterized using bed roughness length (z_0), which was set to 0.7 mm, a representative value for muddy sand substrates (Soulsby, 1983).

To reproduce the competition between tidal and baroclinic forces in the estuarine channel, the model was forced with semidiurnal tides at the seaward shelf boundary and freshwater inflow at the head of the estuary. The salinity of the adjacent coastal ocean was set to 35 g/kg. Neumann-type boundary conditions were applied at the cross-shelf boundaries, imposing a zero-gradient in sea surface elevation along the shore.

Fourteen numerical experiments were implemented, each forced by a single M_2 tidal constituent but differing in depth, channel geometry, river discharge, and tidal amplitude (Table 1). These experiments were designed to examine the sensitivity of estuarine dynamics and the performance of Fr_t under varying physical and forcing conditions. The Reference experiment (or 'Ref') served as the baseline case against which all sensitivity experiments were compared. Four scenario groups were defined as follows. Scenario 1 explored Tidal Variability (Exp 1a–1d, and the Ref); Scenario 2 investigated Depth Variations (Exp 2a–2d, and the Ref); Scenario 3 varied Cross-Channel Slope (Exp 3a,3b, and the Ref); and Scenario 4 analyzed River Discharge (Exp 4a–4c, and the Ref). An additional experiment included both M_2 and S_2 constituents to reproduce a neap–spring tidal cycle and further assess the applicability of Fr_t over a fortnight scale.

The model was initialized from rest and run for six months, allowing sufficient time for steady-state circulation and salinity distribution to develop throughout the estuarine domain (Khosravi et al., 2025). For the four scenario groups forced solely by the M_2 tidal constituent, the last 12.5 h cycle of each simulation was analyzed to assess the ability of Fr_t to diagnose the dominant mechanisms driving the residual flow. For the experiment forced with both M_2 and S_2 constituents, the analysis was

Table 1
Summary of model experiments and boundary forcing conditions. Parameters varied across scenarios are shown in bold red. Q_R and η are river discharge and tidal amplitude, respectively.

Scenario	Experiment	H_{max} (m)	Q_R (m^3/s)	η (m)	c (STD)
Reference	Ref	10	50	1 (M_2)	178
Scenario 1 – Tidal Variability	1a	10	50	**0.2 (M_2)**	178
	1b	10	50	**0.5 (M_2)**	178
	1c	10	50	**1.5 (M_2)**	178
	1d	10	50	**2 (M_2)**	178
Scenario 2 – Depth Variations	2a	**5**	50	1 (M_2)	178
	2b	**7**	50	1 (M_2)	178
	2c	**12**	50	1 (M_2)	178
	2d	**15**	50	1 (M_2)	178
Scenario 3 – Cross-Channel Slope	3a	10	50	1 (M_2)	**203**
	3b	10	50	1 (M_2)	**89**
Scenario 4 – River Discharge	4a	10	**5**	1 (M_2)	178
	4b	10	**10**	1 (M_2)	178
	4c	10	**25**	1 (M_2)	178
Neap–spring tidal cycle	—	10	50	**1 (M_2) + 0.8 (S_2)**	178

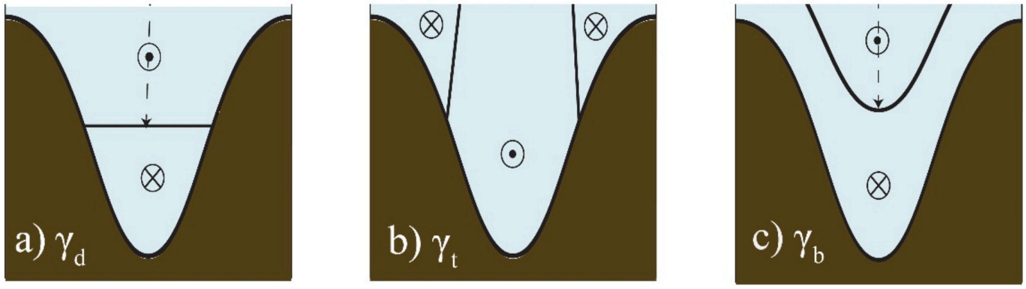

Fig. 2. Transverse structure of residual flow regimes identified through the γ parameter: (a) density-driven γ_d, (b) tidally driven γ_t, and (c) balanced circulation γ_b. Circles with cross indicate inflows, and circles with dot indicate outflows.

based on the last complete fortnightly cycle.

To compare axial salinity gradients between different experiments, results along the estuary are presented as a function of the normalized along-estuary coordinate x/L_s, where x is the distance from the estuary mouth and L_s is the salt intrusion length. Thus, $x/L_s = 0$ corresponds to the estuary mouth and $x/L_s = 1$ denotes the upstream limit of salt intrusion. For convenience, the estuary is subdivided into three regions: the lower estuary (x/L_s = 0–0.25), the middle estuary (x/ L_s = 0.25–0.75), and the upper estuary (x/L_s = 0.75–1).

3.2. Nondimensional parameters: γ, R ratio, and Ri_x

A nondimensional parameter, γ, is used to delineate the boundaries between predominantly barotropic, baroclinic, and near-balanced forcing mechanisms based on the lateral structure of the estuarine residual flow. It is defined as (Khosravi et al., 2025):

$$\gamma = \text{sign}(u_{sh})\left(\frac{e^{(\xi_{up}-1)} + e^{(\xi_{low}-1)}}{2}\right) \tag{8}$$

where u_{sh} is the residual flow over the shoals, and ξ_{up} and ξ_{low} represent the normalized upper and lower limits of the inflow layer within the thalweg, respectively. The parameter ranges from -1 to $+1$. The γ parameter provides a quantitative diagnostic for identifying specific canonical residual-flow structures, including tidally driven circulation ($\gamma_t \approx 0.37$, characterized by outflow in the deep channel and inflow over the shoals), density-driven circulation ($-1 \le \gamma_d < -0.68$), and near-balanced circulation ($0.68 \le \gamma_b \le 1$) (Fig. 2; Khosravi et al., 2025).

Following Khosravi et al. (2025), the present study uses the nondimensional ratio R to identify the main driver of residual flows. R is defined as the ratio of barotropic to baroclinic forcing along the thalweg, where baroclinicity is strongest (Li et al., 1998). It is calculated as:

$$R = \frac{\langle u\,\partial_x u\rangle + \langle v\,\partial_y u\rangle + \langle g\,\partial_x \eta\rangle}{\langle \frac{g}{\rho_0}\int_{-z}^{\eta} \partial_x \rho\; dz\rangle} \tag{9}$$

where the numerator represents the barotropic forcing, including the axial advective tidal stress terms $\langle u\partial_x u\rangle$ and $\langle v\partial_y u\rangle$, and the surface slope term $\langle g\partial_x \eta\rangle$. The denominator represents the baroclinic forcing term. In this formulation, z is the vertical coordinate (positive upward, with the origin at the surface); η is the water level; and v is the tidally varying current in the y-direction. River discharge contributes to both components by enhancing the surface slope (barotropic forcing) and strengthening the density-driven circulation (baroclinic forcing). All terms are directly computed from the model output fields, and angle brackets denote temporal averaging over the tidal cycle. This formulation provides a nondimensional measure of the relative importance of barotropic versus baroclinic forcing and allows assessment of the corresponding tidal Froude number Fr_t. Although evaluated at the thalweg, this choice is consistent with Khosravi et al. (2025), where γ was used to classify residual-flow structures based on lateral patterns in symmetric estuaries. In that framework, the present formulation of R shows systematic agreement with the γ -based regimes. In particular, $|R|\gg1$ corresponds to barotropic-dominated conditions, while $|R|\ll1$ indicates baroclinic dominance, consistent with the γ classification. This supports the use of thalweg-based diagnostics as a compact proxy for the dominant forcing mechanism in idealized symmetric estuaries, although this correspondence may weaken in more asymmetric or rotational settings. A comparison with a laterally averaged formulation of R yields consistent regime transitions, indicating that the results are not sensitive to the thalweg-based evaluation. For each experiment listed in Table 1, the salinity gradient was first normalized by its maximum value along the salinity intrusion length. The normalized along-estuary coordinate (x/L_s) was then divided into 20 equally spaced bins spanning the range of observed values. Within each bin, the normalized salinity gradient values ($\partial S/\partial x$) were summarized using the median, defined as the central value of the ordered data within each bin. The minimum, maximum, and mean values were also computed to characterize the variability of the salinity gradient within each bin. All grid-scale values of Fr_t and R were grouped according to the bin in which their x/L_s position fell. The base-10 logarithm of the absolute values of both Fr_t and R was computed, i.e., $\log_{10}(|Fr_t|)$ and $\log_{10}(|R|)$, for scaling purposes. Hereafter, unless otherwise specified, Fr_t and R refer to these log-transformed quantities. The interpretation is therefore performed in log space: positive values correspond to original magnitudes satisfying $|Fr_t|\gg1$ and $|R|\gg1$, indicating a tendency toward tidal conditions, whereas negative values correspond to $|Fr_t|\ll1$ and $|R|\ll1$, indicating a tendency toward density-driven conditions. Values near zero represent transitional conditions in which neither forcing is clearly dominant. Within each bin, statistical quantities were computed, including the percentage of sign disagreement between Fr_t and R, defined as cases where the two terms had opposite signs. In addition, the absolute discrepancy was calculated as $|Fr_t - R| \times 100$, providing a magnitude-based measure of deviation between the two terms.

To investigate the sensitivity of Fr_t to different density length scales, multiple values of L_ρ were tested as fractions of L_s, ranging from 0.1 L_s to 1 L_s. Each fraction represents the spatial extent from the estuary mouth to a given distance along the channel. By linking the density length scale to the salinity intrusion length, this method provides a systematic and physically consistent framework to evaluate how Fr_t varies with changes in the characteristic density scale along the estuary.

To support the interpretation of the R-based analysis of the barotropic–baroclinic competition that drives residual flow regimes, the horizontal Richardson number (Ri_x, or Simpson number) was also evaluated along the thalweg (Stacey et al., 2001). Ri_x quantifies the strength of the vertical stratification through the ratio between baroclinic straining and tidal mixing (Li et al., 2018):

$$Ri_x = \frac{\beta g \left(\frac{\partial S}{\partial x}\right) H^2}{C_d U_{dT}^2} \tag{10}$$

where the saline expansivity β is taken as 7.7×10^{-4} (g/kg)$^{-1}$, S is the depth-mean subtidal salinity, C_d(= 0.0022 in the present model) is a

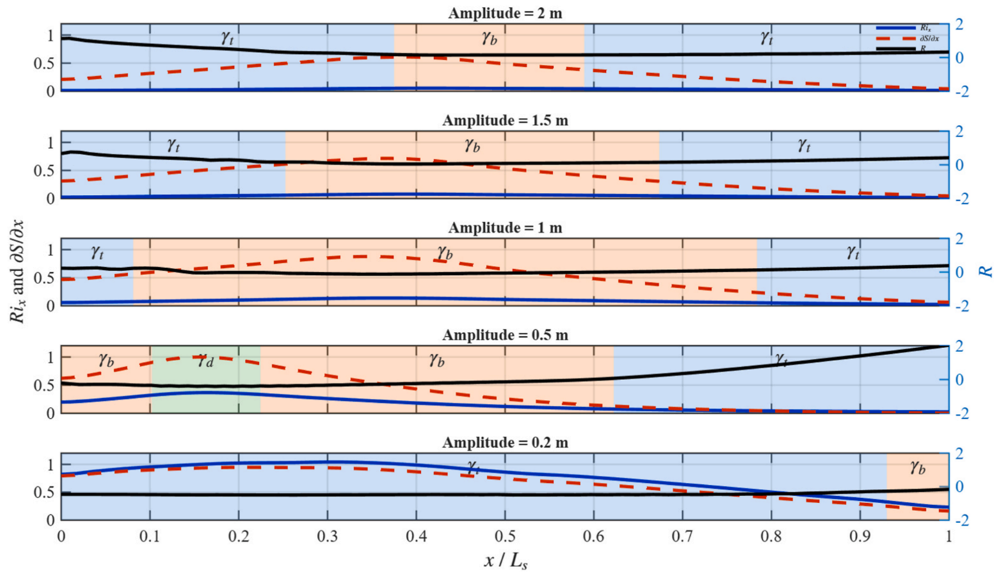

Fig. 3. Scenario 1: line plots show the spatial variation of Ri_x (blue solid line) and the normalized salinity gradient $\partial S/\partial x$ (red dashed line) on the left axis, and the R ratio (black line) on the right axis along the normalized estuarine coordinate x/L_s. Distinct along-estuary dynamical regimes are identified using shaded regions: γ_t (blue shading; tidally driven), γ_d (green shading; density-driven), and γ_b (orange shading; near-balanced conditions). (For interpretation of the references to color in this figure legend, the reader is referred to the Web version of this article.)

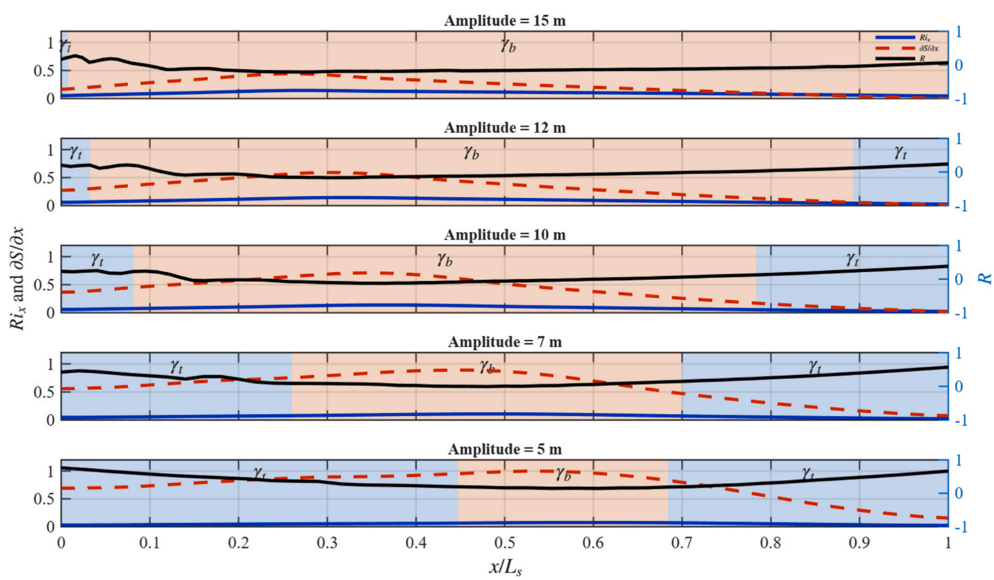

Fig. 4. Same as Fig. 3, but for scenario 2.

bottom drag coefficient, and U_{dT} is the amplitude of the depth-averaged tidal flow. $Ri_x \ll 1$ denotes weakly stratified conditions, while stratification tends to develop as Ri_x approaches unity (Li et al., 2018).

4. Results

4.1. Scenario outputs

4.1.1. Scenario 1- tidal modulation

The experiments with variable tidal forcing reveal three distinct lateral structures—γ_d, γ_t and γ_b (Fig. 3). As tidal amplitudes increase, the subtidal transverse circulation evolves from a γ_d-dominated regime (i.e., density-driven) to one increasingly characterized by γ_t (tidally driven). This progression is reflected clearly in the spatial pattern of the R ratio: γ_t regions exhibit consistently elevated values (mean $R \approx 0.41 \pm 0.4$), γ_b regions show weakly negative mean values ($\approx -0.07 \pm 0.04$), and γ_d regions maintain strongly negative and remarkably stable mean values ($\approx -0.47 \pm 0.04$). Salt intrusion is about 19 km under weak forcing, increases to ~33 km with moderate tides (0.5 m), decreases to ~25 km at 1 m tidal amplitude, and then increases again to ~37 km under strong tides (1.5–2 m). The peak magnitude of the depth-averaged salinity gradient is consistent across all experiments and occurs near the minimum of the R ratio, typically within the γ_d or γ_b regions. This location corresponds to the area of strongest baroclinic forcing and coincides with maximum stratification, as indicated by Ri_x. Upstream, vertical stratification gradually decreases, and the estuary transitions from strongly stratified conditions (Ri_x slightly exceeding unity) to well-mixed conditions ($Ri_x < 0.1$).

4.1.2. Scenario 2- depth variation

These experiments delineate two distinct transverse = structure regimes, γ_t (tidally-driven) and γ_b (balanced, Fig. 4). As estuarine depth

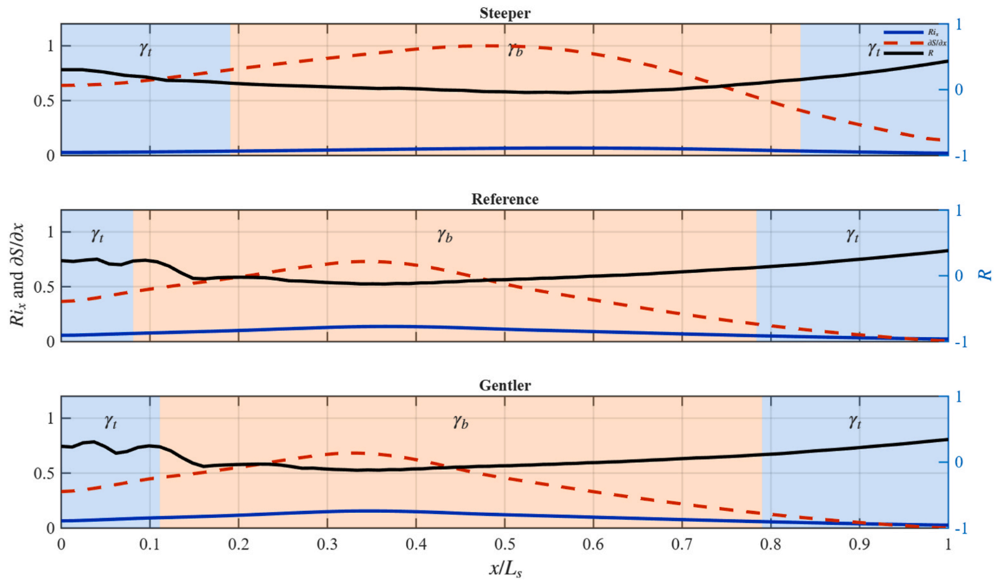

Fig. 5. Same as Fig. 3, but for scenario 3.

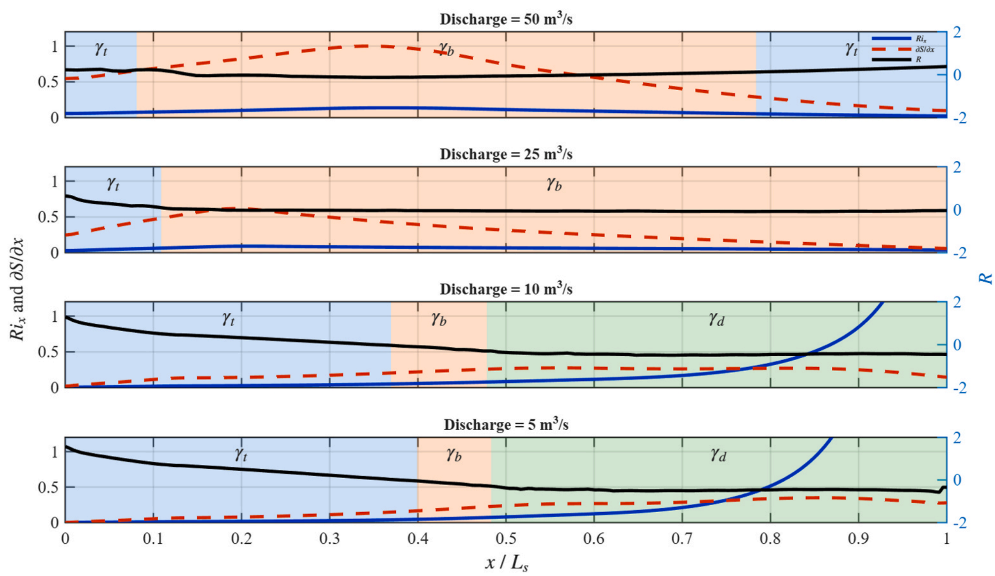

Fig. 6. Same as Fig. 3, but for scenario 4.

increases, the γ_t-dominated regions progressively shrink and are replaced by γ_b structures. This transition is clearly reflected in the spatial pattern of the mean R ratio: γ_t regions exhibit positive R mean values ($\approx 0.30 \pm 0.15$), while γ_b zones show near zero mean values ($\approx 0.05 \pm 0.06$). These dynamic adjustments accompany changes in longitudinal salt transport, extending the salinity intrusion length from 13 km at the shallowest depth to 42 km at the greatest depth. The spatial ordering of peak salinity gradient magnitude mirrors that of Scenario 1, occurring near the minimum R-ratio zone within the γ_b region. The estuary remains vertically well mixed ($Ri_x < 0.15$), with peak salinity gradients collocated with Ri_x maxima.

4.1.3. Scenario 3 – Influence of lateral slope

Scenario 3 also produces the two transverse structures γ_t and γ_b (Fig. 5). The structure γ_b occupies most of the intrusion length, while γ_t is restricted to the mouth and head areas. Increasing the estuarine side slope minorly modifies the spatial extent of these structures. The mean R ratio further highlights this distinction, with γ_t regions showing moderate mean values ($\approx 0.18 \pm 0.08$), in contrast to γ_b regions where the ratio remains near mean zero ($\approx +0.07 \pm 0.06$). The salinity intrusion shortens from ~27 km to ~14 km with increasing cross-channel slope, probably due to the reduction of the deep-channel cross-section. The estuary remains well mixed for all experiments. As with previous scenarios, the peak salinity gradient magnitude is located near the minimum R-ratio (within the γ_b region) where stratification (Ri_x) is maximum.

4.1.4. Scenario 4 - Influence of river discharge

Across all experiments in Scenario 4, three lateral structure regimes emerge—γ_d, γ_t and γ_b (Fig. 6). As river discharge increases, the γ_d structure, that develops for low freshwater input, progressively reduces in extension and eventually disappears, giving way to γ_t–γ_b patterns at higher discharges. The regime-dependent structure is also evident in the mean R ratio, with distinctly positive mean values in γ_t regions ($\approx 0.44 \pm 0.33$), mean values close to zero in γ_b areas ($\approx -0.06 \pm 0.04$), and markedly negative mean values in γ_d zones ($\approx -0.51 \pm 0.03$),

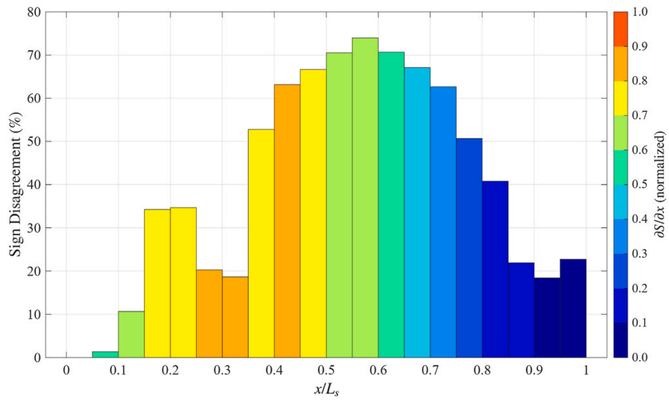

Fig. 7. Sign disagreement between the Fr_t and the R ratio as a function of normalized position (x/L_s). Each bar represents the percentage of cases across all experiments within a given L_s bin where the two parameters have opposite signs. Discrete bar colors indicate the corresponding average of normalized salinity gradient (∂S/∂x). (For interpretation of the references to color in this figure legend, the reader is referred to the Web version of this article.)

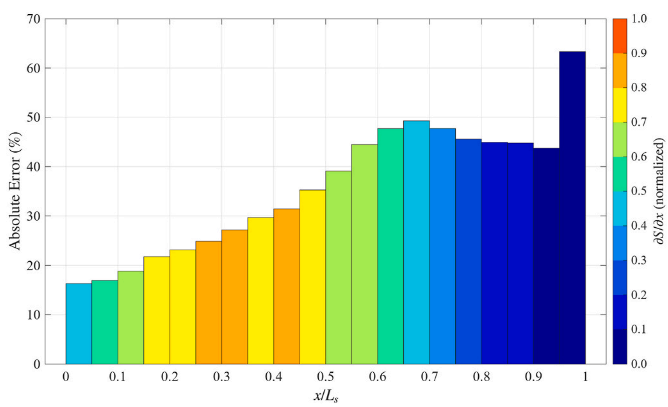

Fig. 8. Absolute error between Fr_t and the R ratio as a function of normalized position (x/L_s), analogous to Fig. 7.

reflecting the differing dynamical characteristics of each regime. At low discharges, Ri_x appears very high near the estuary head due to near-zero tidal velocities, representing a mathematical artifact rather than actual stratification. As discharge increases, Ri_x remains below 0.2, indicating well-mixed conditions. The salinity intrusion length decreases from 79 km to 25 km with increasing freshwater advection. At the lowest discharges (5 and 10 m^3/s), the peak salinity gradient occurs near the estuary head, whereas at higher discharges (25 and 50 m^3/s), it is observed along the first half of the salinity intrusion length. As in previous scenarios, the peak corresponds to the minimum R ratio and maximum stratification —typically within the γ_d or γ_b regions.

4.2. Application of Fr_t at the grid scale

When Fr_t and R have the same sign, they indicate the same dominant driver of residual circulation. Sign comparisons between R and Fr_t (Fig. 7), evaluated at the grid scale ($\Delta x = 333$m) across all experiments, reveal that sign disagreement is lowest near the estuary mouth ($x/L_s = 0$-0.35, <35%) and again near the upper limit of the salinity intrusion ($x/L_s = 0.85$-1, <25%). In contrast, the mid-estuary region exhibits the highest disagreement, exceeding 50%. Over $x/L_s = 0$–0.35, the bin-averaged normalized salinity gradient remains strong at approximately 0.9. This shows that the salinity gradient is highest in the lower estuary (orange) and lowest in the upper estuary (dark blue), as indicated in Fig. 7. Consequently, the upper estuary is not representative of the salinity-gradient conditions along most of the estuarine channel. Furthermore, the absolute discrepancy between Fr_t and R increases toward the upper estuary, with the lowest values (<30%) found over $x/L_s = 0$–0.4, just seaward of the salinity-gradient peak (Fig. 8). In contrast, the upper stretch of the salinity intrusion exhibits the largest absolute discrepancy (>60%), coinciding with the regions of the weakest salinity gradient. The large absolute disagreement between Fr_t and R in the upper estuary (Fig. 8) reinforces the earlier observation (Fig. 7) that this area is unsuitable for exploring Fr_t due to its relatively weaker salinity gradient.

4.3. Fr_t sensitivity to the density length scale

The analyses in the previous section showed that Fr_t, when computed using a density length scale at the grid resolution, identifies better the main driver of residual flow in regions characterized by strong salinity gradient, particularly over the seaward side of the salinity gradient peak. The question arises as to how large this scale could be to yield correct predictions of the dominant residual flow driver. Overall, when L_ρ was set to its smallest value (0.1 L_s), the sign of Fr_t was concordant with the sign of R, indicating that correct driver diagnosis was achieved by Fr_t across the entire experiments (Fig. 9). However, as L_ρ increased, the diagnosed driver by Fr_t progressively deteriorated. Discrepancies between Fr_t and R increased with larger L_ρ (Fig. 10a), while the Pearson correlation coefficient gradually decreased (Fig. 10b), indicating reduced agreement at large density length scales.

The cases with dominant baroclinic (Exp. 1a) and barotropic (Exp. 1c and d) forcing, with no axial change in the main driver of the residual flow, were correctly diagnosed by Fr_t through all examined length scales (Fig. 9). Thus, in regimes where a dominant behaviour clearly emerges, Fr_t remains robust regardless of the density length scale used. Misclassification by Fr_t occurred only when the averaged R along the selected density length scale fell within the near-balanced regime ($-0.2 < R < 0.05$; see Fig. 9). This range represents a dynamic balance where, at R = -0.2, baroclinic forces exceed barotropic forces by a factor of approximately 1.6, whereas at R = 0.05, barotropic forces slightly dominate, exceeding baroclinic forces by a factor of about 1.1. Because R represents the mean axial forcing over each L_ρ, this range may indicate a switch in the dominant driver along L_ρ. The nondimensional Fr_t shows the smallest discrepancies (<30%) for $L_\rho \leq 0.5\ L_s$ (except in Exps. Ref., 3a, 2c, and 2d; see Fig. 9). At these scales, the system is nearly balanced, with a slight dominance of baroclinic forcing ($-0.16 < R < 0$). However, while the shortest L_ρ scales yield the best agreement, measuring axial gradients in the field over small distances (e.g., $0.1L_s$) might be challenging, due for example to salinity variability across the channel or insufficient instrument (e.g., CTD) resolution. L_ρ must be large enough to reduce measurement error and yield a bulk Fr_t. The main challenge is choosing a length scale that is practical for field observations but does not span regions where the dominant driver shifts.

4.4. Definition of a bulk Fr_t parameter

The analysis in Section 4.3 demonstrates that selecting L_ρ within the interval 0-0.5L_s yields the smallest Fr_t errors when identifying the dominant driver of the residual flow (Figs. 9 and 10). Complementary evidence from Section 4.2 further shows that Fr_t remains highly reliable on the seaward side of the peak salinity gradient (L_{pk}), as indicated by the consistently low sign-disagreement and absolute-error percentages in this region (Figs. 7 and 8). This reliability is further supported by the fact that the average dominant residual-flow driver (indicated by the R ratio) remains largely uniform from the estuary mouth to L_{pk} across all experiments (Figs. 3–6), a consistency that is essential for a generally reliable diagnosis within the present experiments.

Across all model configurations, L_{pk} spans a range from as low as 0.17 L_s (Exp. 1b) to as high as 0.9 L_s (Exps. 4a and 4b). This variability implies

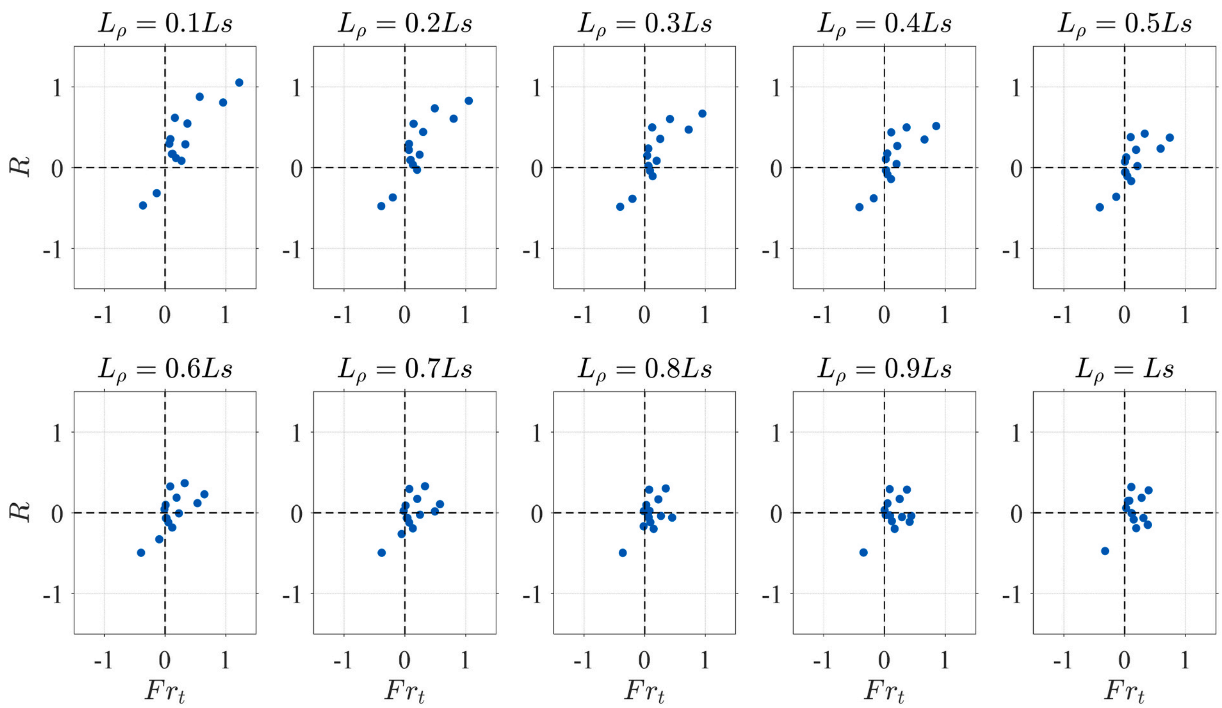

Fig. 9. Comparison of Fr_t ($L_\rho = 0.1L_s$, 0.2 L_s, …, L_s) and R across the first 14 experiments. Each data point represents an individual experiment described in Table 1.

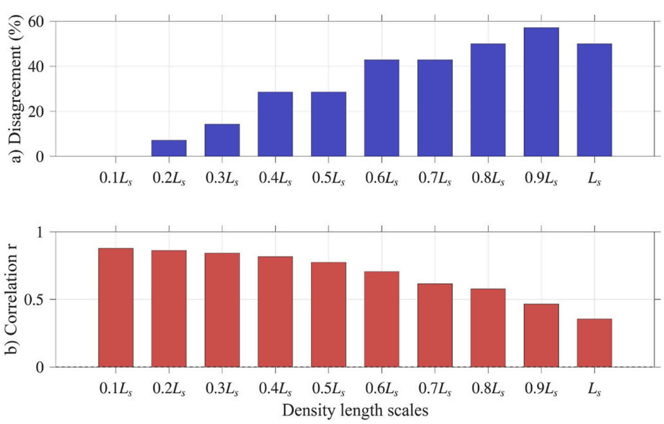

Fig. 10. (a) Percentage of mismatched signs between Fr_t and R relative to the total number of evaluated cases (14 experiments). Each bar represents a density length scale and indicates the cases where Fr_t and R show opposing forcing conditions. (b) Linear correlation coefficient between the predicted Fr_t and R for each density-length scale in (a). The Pearson coefficient quantifies the degree to which variations in Fr_t explain the variability in R, independent of absolute magnitude.

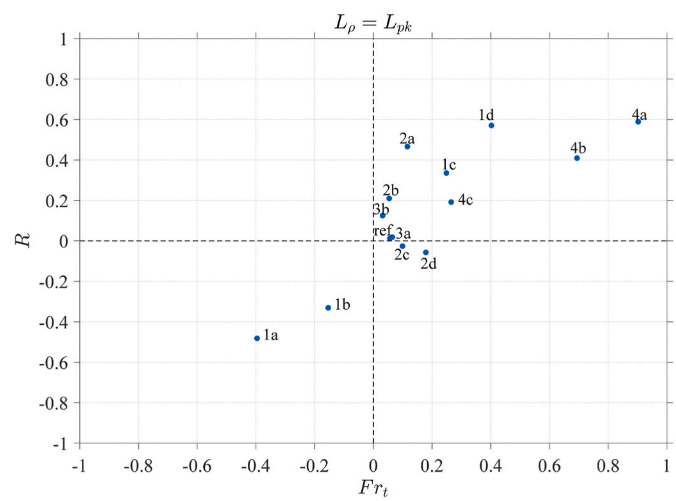

Fig. 11. Comparison of Fr_t ($L_\rho = L_{pk}$) and R across the first 14 experiments. Each data point is labeled with the corresponding experiment number.

that certain density length scales falling outside the optimal 0-0.5 L_s interval identified in Section 4.3—specifically those with 0.5 $L_s < L_{pk} <$ 0.9L_s—can still produce a reliable Fr_t diagnosis. Taken together, these findings motivate a broader question: can the full estuarine region—from the mouth, or more precisely from the point where the axial salinity gradient first becomes non-zero (to avoid for example the flat gradient that may be produced at the entrance by seawater intrusion), to L_{pk}—serve as an effective density length scale for defining Fr_t as a single bulk parameter capable of consistently identifying the dominant forcing mechanism? Across all experiments conducted here, this spatial length exhibits a predominantly linear salinity gradient (Figs. 3–6), meaning that salinity changes with distance at an approximately constant rate over this length scale.

When $L_\rho = L_{pk}$, Fr_t successfully identifies the dominant driver indicated by the mean R-ratio (Fig. 11). While some near-balanced cases, such as Exp. 2c and 2d ($-0.06 < \mathrm{R} < 0$), represent exceptions, Fr_t still correctly diagnoses the dominant driver for other near-balanced cases, including the reference experiment and Exp. 3a ($0 < R < 0.02$). In these two cases, Fr_t ranges between 0 and 0.18, suggesting a slight barotropic dominance (barotropic forcing exceeds baroclinic forcing by roughly 1.5 times at $Fr_t = 0.18$), whereas the R values indicate a slight baroclinic dominance (baroclinic forcing exceeds barotropic forcing by about 1.1 times at $R = -0.06$).

In essence, Fr_t yields a reliable indication of the dominant subtidal forcing only when the density length scale is chosen appropriately. The analyses above show that this requirement is met when L_ρ falls within the interval from the estuary mouth to the peak salinity gradient (0- L_{pk}) or, equivalently, when any length scale within the optimal 0-0.5 L_s range is used. Although Fr_t may occasionally fail under near-balanced condi-

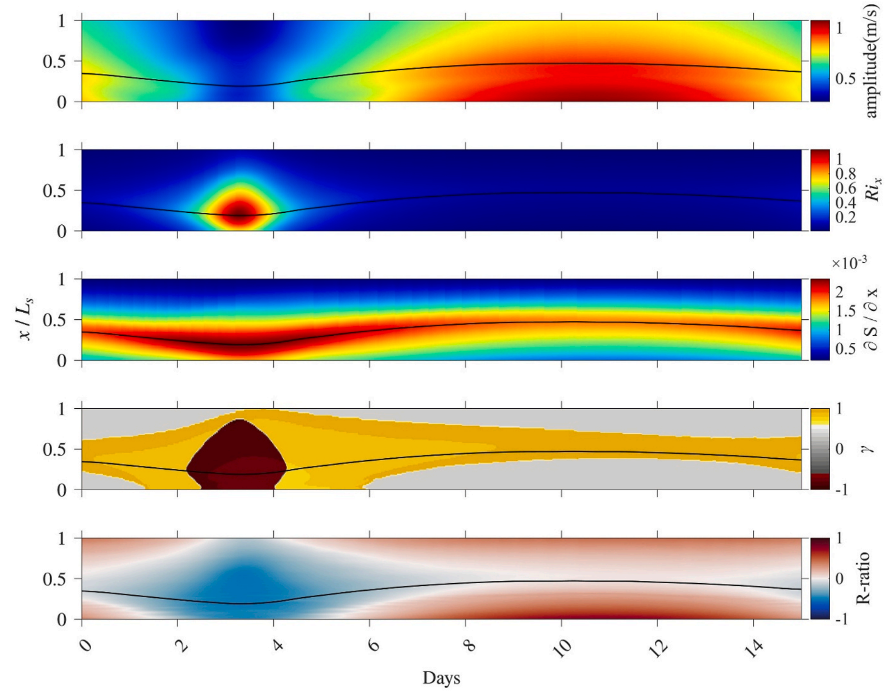

Fig. 12. Fortnightly variability of key estuarine dynamics along the normalized estuarine coordinate x/L_s at the thalweg: a) cross-channel averaged surface tidal amplitudes, b) stratification, c) axial salinity gradients, d) transverse residual flow structure, and e) R-ratio. The solid black line represents the location of the maximum horizontal salinity gradient.

tions even when these density length scales are used, the diagnostic remains largely reliable for relatively dominant barotropic or baroclinic regimes. Consequently, depending on whether L_s or L_{pk} is available, one may select either the distance from the first non-zero salinity gradient at the estuary mouth to L_{pk} or the fixed fraction 0.5 L_s. Within the present idealized experiments, both choices yielded generally consistent Fr_t-based diagnoses of the dominant residual-flow driver. These findings suggest that Fr_t is most appropriately interpreted as an emergent diagnostic parameter reflecting the established salinity structure and the balance between barotropic and baroclinic forcing, rather than as an independent governing control on estuarine dynamics. The next section provides an example of application of the above findings.

For field applications, the along-estuary salinity distribution should ideally be measured to identify the location L_{pk}. These salinity profiles acquired using a CTD along a gridded spatial transect from $x/ L_s = 0$ to $x/L_s = 1$ (e.g., where salinity decreases below 1 g/kg), can be conducted using a fast-moving boat following the high-water slack, similar to the field surveys described by Garel et al. (2025). High-water slack is preferred because salt intrusion typically reaches its maximum landward extent during this phase of the tidal cycle. If the tidal excursion length is known, the low-water-slack salinity distribution may be approximated by shifting the high-water-slack profile seaward by one tidal excursion. Assuming limited intratidal deformation, the high- and low-water-slack salinity distributions can then be used to estimate the tidally averaged salinity field and the corresponding peak salinity gradient location, providing a practical estimate of the density length scale L_ρ. Nevertheless, uncertainties may still arise under near-balanced forcing conditions.

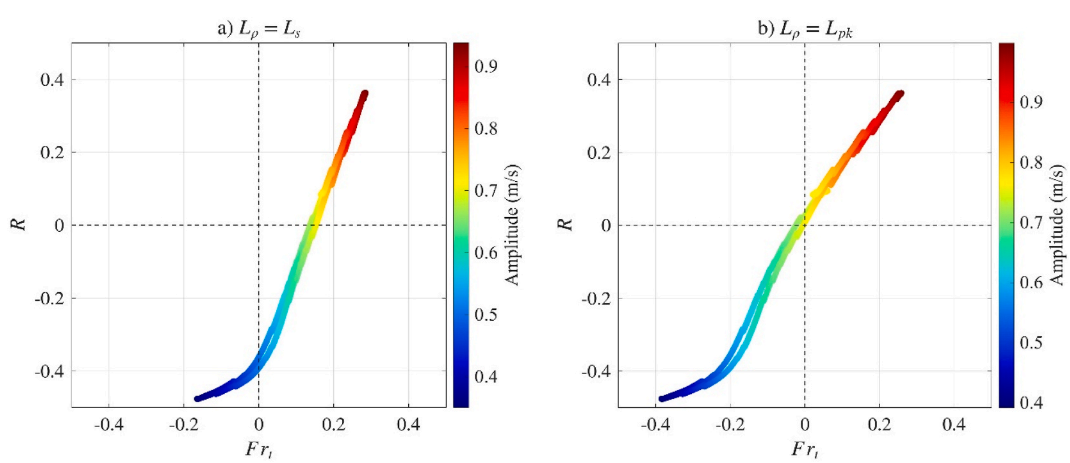

Fig. 13. Comparison of Fr_t and R over a fortnight scale for a) $L_\rho = L_s$ and b) $L_\rho = L_{pk}$. Each dot represents a specific tidal velocity amplitude (color-coded), showing how Fr_t and R vary across the range of tidal forcing. (For interpretation of the references to color in this figure legend, the reader is referred to the Web version of this article.)

4.5. Fortnightly diagnosis of Fr_t

Over the fortnightly cycle (experiment 15), the maximum tidal velocity at the estuary mouth varies between 0.4 m/s (day 3) and 1.1 m/s (day 11), corresponding to neap and spring tides, respectively (Fig. 12a). These amplitudes slightly attenuate toward the limit of the salinity intrusion where they reach 0.3 m/s (day 3) and 0.8 m/s (day 11). Increasing tidal amplitude drives the salt intrusion further landward, extending its length from 22 km at neap tide to 27 km at spring tide. A stratified state ($0.9 < Ri_x < 1.15$) develops primarily in the lower estuary ($x/L_s = 0.2$) near neap tide, while well-mixed conditions ($Ri_x < 0.7$) prevail elsewhere along the estuary and throughout the rest of the tidal cycle (Fig. 12b). The maximum salinity gradient varies between the lower estuary at neap tide (0.0023 g/kg/m at $x/L_s = 0.2$) and the mid-estuary at spring tide (0.0018 g/kg/m at $x/L_s = 0.47$; Fig. 12c). The peak Ri_x occurs slightly upstream of the maximum salinity gradient because tidal velocity decreases landward, increasing Ri_x even as the salinity gradient begins to weaken (see Eq. (10)).

The competition between forcings along the estuary produces three lateral flow structures in residual flow—γ_t, γ_d, and γ_b—with corresponding barotropic–baroclinic ratios $R > 0.08$, $R < -0.45$, and $-0.45 < R < 0.08$, respectively (Fig. 12d and e). At each time step, the lowest R values, marking peak baroclinic influence, coincide with the maximum salinity gradient (see solid line in Fig. 12e). The average dominant forcing remains generally constant from the mouth up to the vicinity of this gradient maximum, except for intermediate tides (e.g., between days 0-2 and 5-8; Fig. 12e) when the lower estuary transits from a baroclinic to barotropic regime.

Assuming $L_\rho = L_s$, Fr_t fails to capture the dominant exchange mechanism during a substantial part of the fortnightly cycle—when tidal velocities are 0.5–0.7 m/s around days 2 and days 5 (~22% of the cycle, Fig. 13a). At that time, the R ratio ($-0.38 < R < 0$) indicates that baroclinic forces can exceed barotropic forces by a factor of up to 2.4, yet Fr_t (0–0.15) misleadingly suggests barotropic dominance (~1.4×baroclinic forcing). The $L_\rho = L_s$ assumption underestimates baroclinic forcing and misidentifies the dominant mechanism because the primary driver of the residual flow varies along the estuary. When these spatially alternating drivers are averaged over L_s, their opposing contributions largely cancel out, yielding values that falsely indicate a balanced or weakly forced system (Fig. 12e).

When considering $L_\rho = L_{pk}$ (Fig. 13b), Fr_t correctly identifies the dominant exchange mechanism for most of the fortnightly cycle. It fails only briefly (~1.5% of the time series) around days 1 and 6, when mean R values are nearly zero. During these periods, the R ratio averaged over L_ρ ranges between 0 and 0.02, indicating slight barotropic dominance (~1.05× the baroclinic forcing), whereas Fr_t points to a weak baroclinic influence (~1.007× the barotropic forcing). These discrepancies occur in regions where the main drivers of the residual flow are nearly balanced (Fig. 12e and. 13b). When a smaller density length scale is adopted, the resulting error remains consistently on the order of ~1.5%

5. Discussion

The densimetric tidal Froude number (Fr_t) has been calculated using different definitions of the density length scale (L_ρ) in previous studies (Cho et al., 2020; Garel et al., 2025; Valle-Levinson and Schettini, 2016; Winant et al., 2003). When the density gradient is approximately linear, the specific choice of L_ρ has little influence on Fr_t. However, the present results indicate that this assumption does not always hold. In cases where the density gradient varies nonlinearly, the smallest relevant length scale should ideally be used to properly represent the gradient. In practice, however, such small scales on the order of hundreds of meters are not always feasible to apply, and therefore a larger L_ρ must often be adopted, covering a sufficiently long segment where the salinity gradient is approximately linear. The present study indicates that selecting this stretch on the seaward side of the salinity-gradient peak generally ensures that the dominant forcing remains consistent across that distance and that Fr_t provides a process-based diagnostic of residual-flow control. Using L_ρ larger than the salinity-gradient peak can misidentify the dominant residual-flow driver because large-scale averaging mixes baroclinic and barotropic effects, resulting in near zero Fr_t values. Alternatively, a near-zero Fr_t may reflect an actual balance between barotropic and baroclinic forcing over the selected segment, yielding no clear indication of dominance. The sensitivity of Fr_t to the density length scale was also highlighted by Garel et al. (2025), who showed that using the full salinity-intrusion length can obscure the dominant residual-flow driver because the salinity gradient is highly nonlinear along the estuary, causing the averaged gradient to misrepresent local baroclinic forcing, overestimate density effects, and mask periods when tidal stress dominates.

In the present study, the competition between barotropic–baroclinic forcings shaping the residual circulation is assessed along the channel using the R ratio. Residual-flow regimes were identified independently using the γ parameter together with the R ratio (Section 3.2), and the

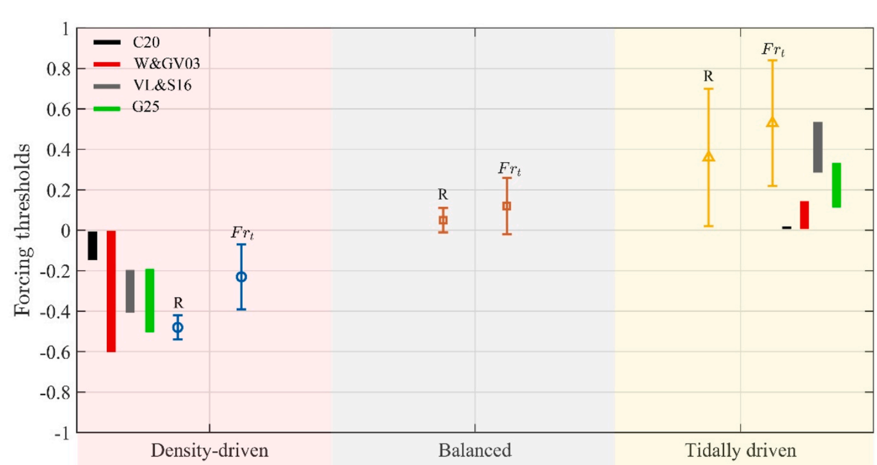

Fig. 14. Mean values (colored markers) of the R ratio and Fr_t across all experiments, with bars indicating one standard deviation. Shaded backgrounds indicate regimes dominated by balanced (light grey), tidal (yellow), and density-driven (pink) lateral structures. The vertical-colored bars denote previously proposed Fr_t ranges for tidally driven and density-driven lateral structures from the literature: VL&S16 (grey; Valle-Levinson and Schettini, 2016), C20 (black; Cho et al., 2020), W&GB03 (red; Winant et al., 2003), and G25 (green; Garel et al., 2025). (For interpretation of the references to color in this figure legend, the reader is referred to the Web version of this article.)

corresponding Fr_t values were subsequently compiled for each dynamically identified regime across all experiments. Distinct ranges of the R within the present experiments are associated with different lateral structures of the axial residual flow: tidally driven regions show the highest mean R values (0.36 ± 0.34), balanced regions exhibit small positive mean values (0.05 ± 0.06), and density-driven regions are strongly negative mean values (-0.48 ± 0.06) (Fig. 14). An overlap ($R = 0.02$–0.11) marks the transition where neither process clearly dominates. However, although the R ratio can be readily obtained from the momentum terms in model outputs, observational studies typically lack direct access to these forcing components. In such cases, the tidal Froude number (Fr_t) provides a practical diagnostic for assessing the relative influence of tidal and density-driven mechanisms. Fr_t characteristic values for tidally driven, density-driven, and balanced conditions were therefore established. Within the present experiments, tidally driven circulation occurs at high Fr_t mean values (0.53 ± 0.31), density-driven circulation emerges at low Fr_t mean values (-0.23 ± 0.16), and near-balanced regimes occupy a narrow transitional range mean values (0.12 ± 0.14), where neither process clearly prevails (Fig. 14). The interval $Fr_t = 0.22$–0.26 marks an overlap where tidally driven and nearly balanced conditions coexist. The values shown in Fig. 14 represent empirical regime-associated ranges (mean ± standard deviation) within the present idealized configuration, rather than strict or universally applicable thresholds, and may vary with estuarine geometry, forcing conditions, turbulence parameterization, and other physical processes not considered here. Nevertheless, these regime-associated ranges are compared below with values reported for real estuaries to assess their broader physical relevance.

In a highly seasonal tropical system, the Mossoró Estuary, Valle-Levinson and Schettini (2016) examined fortnightly modulation of subtidal circulation under wet and dry conditions, collecting velocity and salinity at 2 km upstream from the estuary entrance. Considering $L_\rho = L_T$, they analyzed subtidal variability with Fr_t and estimated axial density gradients via $\partial\rho/\partial t = -u\partial\rho/\partial x$. Although the velocity measurements were taken within the first ~2 km, where high-tide salinity appears nearly uniform, the axial salinity profiles had to be shifted seaward by half of the tidal excursion (11.2 km in the wet season and 6.4 km in the dry season) to obtain their subtidal equivalents. After this adjustment, the profiles still display a clear landward salinity gradient, demonstrating that the mooring is in a region of non-uniform subtidal salinity. This indicates that their use of $L_\rho = L_T$ falls within the region where salinity varies at an approximately constant rate on the seaward side of the peak gradient located ~14 km upstream. Furthermore, the Fr_t ranges reported in their study, at both wet and dry seasons, with values above 0.3 indicating advective dominance during spring tides and values below −0.2 indicating baroclinic dominance during neap tides, are consistent with the ranges identified in the present study (Fig. 14).

In the Sumjin River Estuary, Cho et al. (2020) measured currents 7 km upstream of the estuary mouth and salinity along a 12 km reach previously identified as the active mixing zone. Using Fr_t and assuming a density length scale $L_\rho = L_T = 12$ km, they reported stronger baroclinic forces during spring tide ($Fr_t = -0.14$) than during neap tide ($Fr_t = 0.04$), attributing this to stronger exchange flow and horizontal salinity gradients during spring tides (Fig. 14). In light of the presented numerical results, these Fr_t values fall within a range where Fr_t is sensitive to the choice of density length scale and may be prone to misinterpretation. Moreover, their axial salinity surveys show that the peak subtidal salinity gradient occurs at ~10 km of the mouth for both spring and neap tides. During spring tides, the gradient increases steadily to ~2.5 g/kg/km, whereas during neap tides it varies irregularly, rising slightly over the first 4 km, dipping near 9 km, and reaching ~1.5 g/kg/km at 10 km. While using a 12 km density length scale is consistent with the gradient structure during spring tides, the irregular neap tide gradient violates the assumption of a monotonic axial density gradient. Imposing a fixed 12 km scale under these conditions likely leads to misinterpretation of the resulting Fr_t estimates during the neap tide.

In Laguna San Ignacio, an arid lagoon, Winant et al. (2003) measured currents approximately 5 km from the mouth, where the tidal velocity amplitude was 0.56 m/s, corresponding to a tidal excursion of ~8 km. Their study also reported an axial density gradient that increased steadily toward the head at 25 km. They assumed $L_\rho = L_T$ when calculating Fr_t, an assumption supported by the present study, as the main driver of the residual flow over this spatial length scale remains uniform. Furthermore, the Fr_t ranges identified in their study indicate that values between 0 and −0.6 correspond to baroclinic estuarine exchange in Laguna San Ignacio, consistent with the two-layer density-driven exchange flow observed here (Fig. 14). In contrast, Fr_t values between 0 and +0.16 indicate near-balanced residual flow drivers with slight barotropic influence, while a clearly barotropic-dominated regime would require Fr_t values exceeding +0.26.

In low freshwater inflow Guadiana Estuary, (Garel et al., 2025) used vessel- and bottom-mounted ADCP data collected 20 km from the mouth to show a fortnightly reversal in residual circulation: tidal forcing dominates during spring tides, whereas density gradients dominate during neaps. Their axial salinity gradient increased steadily between 4 and 20 km. For Fr_t they assumed the tidal length scale to be the tidal excursion and tested two density length scales. Using the salinity-intrusion length (~30 km) spanned regions where the dominant residual-flow mechanism changes, yielding predominantly baroclinic Fr_t values that masked the observed tidally driven lateral structure in spring tide. Using a shorter density scale of 16 km, matching the salinity-sampling extent, reproduced the switch, consistent with the requirement that the chosen length scale lie entirely within the region where the salinity gradient increases toward its peak at ~20 km. Their Fr_t ranges indicated gravitational circulation for $Fr_t < -0.2$ and tidal dominance for $Fr_t > +0.1$ (Fig. 14). While their baroclinic limit agrees with present results, part of diagnosed barotropic range (0.1–0.26) corresponds to the near-balanced regime identified here; nonetheless, the observed residual structure showed barotropic control, underscoring that Fr_t ranges are not fixed but depend on estuarine conditions.

6. Conclusion

The 3D modelling experiments conducted in an idealized shelf–estuary system enabled a systematic assessment of the densimetric tidal Froude number (Fr_t) as a diagnostic tool for identifying the dominant subtidal circulation driver. The experiments show that Fr_t can reliably distinguish between barotropic and baroclinic control when the density length scale is defined over short distances (order of hundreds of meters). However, the results also reveal that the skill of Fr_t depends strongly on how it is constructed. In particular, using a local density length scale, defined within regions where the axial salinity distribution varies at an approximately constant rate, and evaluating Fr_t seaward of the salinity-gradient maximum, consistently improves the agreement between Fr_t and the diagnosed dominant forcing. Within this zone, the dominant mechanism governing the subtidal circulation remains nearly uniform, allowing Fr_t to provide a useful bulk indication of the prevailing forcing regime. In contrast, defining the density scale using longer distances, such as the full salinity intrusion length, introduces ambiguity because the residual-flow driver may vary across the scale over which Fr_t is computed. By examining mean Fr_t values together with the corresponding lateral structure of the residual axial flow, this study found distinct distributions of Fr_t among the simulated forcing regimes. Tidally driven simulations had a mean Fr_t of 0.53 ± 0.31, density-driven simulations had a mean of -0.23 ± 0.16, and near-balanced simulations had a mean of 0.12 ± 0.14, in which neither process clearly dominates. Accordingly, Fr_t should be viewed primarily as a process-based diagnostic indicator. The reported mean values describe the present idealized configuration and should not be interpreted as universal thresholds for regime classification, as their quantitative values remain configuration-dependent.

CRediT authorship contribution statement

M. Khosravi: Data curation, Formal analysis, Investigation, Methodology, Software, Validation, Visualization, Writing – original draft, Writing – review & editing. **A.B. Fortunato:** Methodology, Software, Supervision, Writing – review & editing. **A. Lopez-Ruiz:** Software, Writing – review & editing. **A. Valle-Levinson:** Conceptualization, Writing – review & editing. **E. Garel:** Conceptualization, Funding acquisition, Methodology, Resources, Supervision, Writing – review & editing.

Declaration of competing interest

The authors declare that they have no known competing financial interests or personal relationships that could have appeared to influence the work reported in this paper.

Acknowledgment

The study is funded by FCT project PTDC/CTA-OHR/4268/2021 - Fortnightly switching of residual flow drivers in estuaries (SWITCH). The funding provided by FCT to the project's LA/P/0069/2020 awarded to the Associate Laboratory ARNET and UID/00350/2020 awarded to CIMA of the University of the Algarve are acknowledged. The authors thank the editor and anonymous reviewers for their constructive comments, which helped improve the manuscript. Finally, Maziar Khosravi thanks his father-in-law, Mr. Mohammadreza Azarbani, for his continuous kindness, support and encouragement.

Data availability

All data and source model files are available from the corresponding author upon request.

References

Burchard, H., Hetland, R.D., Schulz, E., Schuttelaars, H.M., 2011. Drivers of residual estuarine circulation in tidally energetic estuaries: straight and irrotational channels with parabolic cross section. J. Phys. Oceanogr. 41 (3), 548–570.
Cho, E.-B., Cho, Y.-K., Kim, J., 2020. Enhanced exchange flow during spring tide and its cause in the sumjin River estuary, Korea. Estuaries Coasts 43, 525–534.
Deltares, 2013. Delft3D-FLOW User Manual. Deltares, Delft, The Netherlands, p. 330.
Dijkstra, Yoeri M., Schuttelaars, Henk M., Burchard, Hans, 2017. Generation of exchange flows in estuaries by tidal and gravitational eddy viscosity-shear covariance (ESCO). Journal of Geophysical Research: Oceans 122 (5), 4217–4237. https://doi.org/10.1002/2016jc012379. https://agupubs.onlinelibrary.wiley.com/doi/10.1002/2016JC012379. (Accessed 22 May 2017).
Dyer, K.R., 1973. Estuaries: a Physical Introduction, second ed.
Farmer, D.M., Smith, J.D., 1980. Tidal interaction of stratified flow with a sill in Knight Inlet. Deep-Sea Res., Part A 27 (3–4), 239–254.
Friedrichs, C.T., Hamrick, J.M., 1996. Effects of channel geometry on cross-sectional variations in along-channel velocity in partially stratified estuaries. Buoyancy Effects on Coastal and Estuarine Dynamics 53, 283–300.
Gardner, L., Kjerfve, B., 2006. Tidal fluxes of nutrients and suspended sediments at the North Inlet–Winyah Bay National Estuarine Research Reserve. Estuar. Coast Shelf Sci. 70 (4), 682–692.
Garel, E., Khosravi, M., Díez-Minguito, M., Valle-Levinson, A., 2025. Fortnightly switching of residual flow drivers produced by seawater intrusion in a long, non-rotating Estuary. Estuaries Coasts 48 (6), 176.
Garel, E., Ferreira, Ó., 2013. Fortnightly changes in water transport direction across the mouth of a narrow estuary. Estuaries Coasts 36, 286–299.
Geyer, W., 2010. Estuarine salinity structure and circulation. Contemporary Issues in Estuarine Physics 12, 26.
Geyer, W.R., MacCready, P., 2014. The estuarine circulation. Annu. Rev. Fluid Mech. 46 (1), 175–197.
Guha, A., Lawrence, G.A., 2013. Estuary classification revisited. J. Phys. Oceanogr. 43 (8), 1566–1571.
Hansen, D.V., Rattray, Jr M., 1966. Gravitational Circulation in Straits and Estuaries.
Hosseini, S.T., Stanev, E., Pein, J., Valle-Levinson, A., Schrum, C., 2023. Longitudinal and lateral circulation and tidal impacts in salt-plug estuaries. Front. Mar. Sci. 10, 1152625.
Ianniello, J.P., 1977a. Nonlinearly Induced Residual Currents in Tidally Dominated Estuaries. University of Connecticut.
Ianniello, J.P., 1977b. Tidally Induced Residual Currents in Estuaries of Constant Breadth and Depth.
Jay, D.A., Smith, J.D., 1990a. Residual circulation in shallow estuaries: 1. Highly stratified, narrow estuaries. J. Geophys. Res. Oceans 95 (C1), 711–731.
Jay, D.A., Smith, J.D., 1990b. Residual circulation in shallow estuaries: 2. Weakly stratified and partially mixed, narrow estuaries. J. Geophys. Res. Oceans 95 (C1), 733–748.
Khosravi, M., Fortunato, A.B., Lopez-Ruiz, A., Valle-Levinson, A., Garel, E., 2025. Fortnightly variability of the lateral structure of residual flows along non-rotating estuaries. Estuar. Coast Shelf Sci., 109562
Lesser, G.R., Roelvink, J.A., van Kester, J.T.M., Stelling, G.S., 2004. Development and validation of a three-dimensional morphological model. Coast. Eng. 51 (8–9), 883–915.
Li, C., Valle-Levinson, A., Wong, K.C., Lwiza, K.M., 1998. Separating baroclinic flow from tidally induced flow in estuaries. J. Geophys. Res. Oceans 103 (C5), 10405–10417.
Li, X., Geyer, W.R., Zhu, J., Wu, H., 2018. The transformation of salinity variance: a new approach to quantifying the influence of straining and mixing on estuarine stratification. J. Phys. Oceanogr. 48 (3), 607–623.
Li, C., O'Donnell, J., 2005. The effect of channel length on the residual circulation in tidally dominated channels. J. Phys. Oceanogr. 35 (10), 1826–1840.
Li, C., Valle-Levinson, A., 1999. A two-dimensional analytic tidal model for a narrow estuary of arbitrary lateral depth variation: the intratidal motion. J. Geophys. Res. Oceans 104 (C10), 23525–23543.
Officer, C.B., 1976. Physical Oceanography of Estuaries (And Associated Coastal Waters).
Pingree, R.D., Maddock, L., 1977. Tidal residuals in the English Channel. J. Mar. Biol. Assoc. U. K. 57 (2), 339–354.
Pritchard, D.W., 1956. The dynamic structure of a coastal plain estuary. J. Mar. Res. 15 (1), 33–42.
Ross, L., Valle-Levinson, A., Sottolichio, A., Huybrechts, N., 2017. Lateral variability of subtidal flow at the mid-reaches of a macrotidal estuary. J. Geophys. Res. Oceans 122 (9), 7651–7673.
Soulsby, R.L., 1983. The Bottom Boundary Layer of Shelf Seas, 35. Elsevier Oceanography Series, pp. 189–266.
Stacey, M.T., Burau, J.R., Monismith, S.G., 2001. Creation of residual flows in a partially stratified estuary. J. Geophys. Res. Oceans 106 (C8), 17013–17037.
Valle-Levinson, A., 2008. Density-driven exchange flow in terms of the kelvin and ekman numbers. J. Geophys. Res. Oceans 113 (C4).
Valle-Levinson, A., 2021. Dynamics-based classification of semienclosed basins. Reg. Stud. Mar. Sci. 46, 101866.
Valle-Levinson, A., 2022. Introduction to Estuarine Hydrodynamics. Cambridge University Press.
Valle-Levinson, A., Wong, K.C., Lwiza, K.M., 2000. Fortnightly variability in the transverse dynamics of a coastal plain estuary. J. Geophys. Res. Oceans 105 (C2), 3413–3424.
Valle-Levinson, A., Schettini, C.A., 2016. Fortnightly switching of residual flow drivers in a tropical semiarid estuary. Estuar. Coast Shelf Sci. 169, 46–55.
Winant, C.D., Gutié, G., De Velasco, R., 2003. Tidal dynamics and residual circulation in a well-mixed inverse Estuary. J. Phys. Oceanogr. 33 (7), 1365–1379.
Wong, K.C., 1994. On the nature of transverse variability in a coastal plain estuary. J. Geophys. Res. Oceans 99 (C7), 14209–14222.

Update

Estuarine, Coastal and Shelf Science

Volume 341, Issue , 15 October 2026, Page

DOI: https://doi.org/10.1016/j.ecss.2026.110167

Estuarine, Coastal and Shelf Science 341 (2026) 110167

Contents lists available at ScienceDirect

Estuarine, Coastal and Shelf Science

journal homepage: www.elsevier.com/locate/ecss

Corrigendum to "Diagnosis of residual flow drivers in estuaries with the densimetric tidal Froude number" [Estuar. Coast. Shelf Sci. 341 (2026) 110140 DOI of original article: 10.1016/j.ecss.2026.110140]

M. Khosravi [a,e,*], A.B. Fortunato [b], A. Lopez-Ruiz [c], A. Valle-Levinson [d], E. Garel [a]

[a] *CIMA/ARNET, Universidade do Algarve, Faro, Portugal*
[b] *LNEC – Laboratório Nacional de Engenharia Civil, Avenida do Brasil 101, Lisboa, 1700-066, Portugal*
[c] *Departamento de Ingeniería Aeroespacial y Mecánica de Fluidos, Universidad de Sevilla, Camino de los Descubrimientos s/n, Seville, 41092, Spain*
[d] *Civil and Coastal Engineering Department, University of Florida, Gainesville, USA*
[e] *Department of Civil and Resource Engineering, Dalhousie University, 5268 DaCosta Row, Halifax, Nova Scotia, B3H 4R2, Canada*

The authors regret that Fig. 4 in the published article contained an incorrect axis/title label. The label was mistakenly shown as "**Amplitude**" instead of "**Depth**". The corrected version of Fig. 4 is provided with this corrigendum. This correction is limited to the figure label only and does not affect the results, discussion, or conclusions of the paper.

DOI of original article: https://doi.org/10.1016/j.ecss.2026.110140.
* Corresponding author. CIMA/ARNET, Universidade do Algarve, Faro, Portugal.
E-mail addresses: mkhosravi@ualg.pt, maziar.khosravi@dal.ca (M. Khosravi).

https://doi.org/10.1016/j.ecss.2026.110167

Available online 8 August 2026

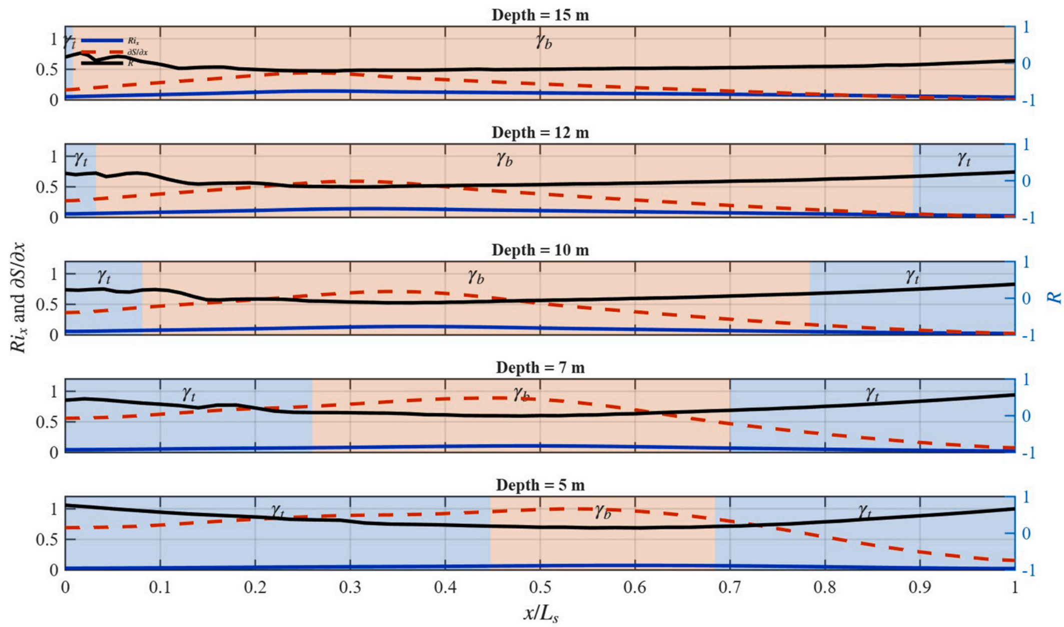

The authors would like to apologise for any inconvenience caused.